

KINEMATIC CONSTRAINTS ON EVOLUTIONARY SCENARIOS FOR BLUE COMPACT DWARF GALAXIES : I. NEUTRAL GAS DYNAMICS

LIESE VAN ZEE

Herzberg Institute of Astrophysics, National Research Council of Canada
 5071 W. Saanich Road, Victoria, BC V9E 2E7 Canada

JOHN J. SALZER^a

^aNSF PRESIDENTIAL FACULTY FELLOW

Astronomy Department, Wesleyan University, Middletown, CT 06459-0123

AND

EVAN D. SKILLMAN

Astronomy Department, University of Minnesota, 116 Church St. SE
 Minneapolis, MN 55455

To appear in the Astronomical Journal

ABSTRACT

We present the results of high spatial resolution HI synthesis observations of six blue compact dwarf (BCD) galaxies. Optically, the selected galaxies have smooth, symmetric isophotes, and thus are the most likely of the BCD class to fade into an object morphologically similar to a dwarf elliptical when the current starburst ends. The neutral gas in all six galaxies appears to be rotationally supported, however, indicating that true morphological transformation from a BCD to a dE will require significant loss of angular momentum. Based on the observed neutral gas dynamics of these and other BCDs, it is unlikely that present-day BCDs will evolve directly into dwarf ellipticals after a starburst phase. We discuss alternative evolutionary scenarios for BCDs and place them within the larger context of galaxy formation and evolution models.

In general, BCDs appear to have steeper rotation curves than similar luminosity low surface brightness dwarf galaxies. BCDs have centrally concentrated mass distributions (stars, gas, and dark matter) and have lower specific angular momenta. Based on disk instability analyses, steeply rising rotation curves result in higher threshold densities for the onset of star formation. These results suggest that angular momenta may play a crucial role in the morphological evolution of low mass galaxies: galaxies with low angular momenta will be able to collapse into small, compact galaxies while galaxies with high angular momenta will be more diffuse systems. Further, because the star formation threshold density is higher in low angular momenta systems, star formation will be delayed until an extremely high surface density is reached. Thus, angular momentum may be the fundamental parameter which determines if a low mass galaxy will have centrally concentrated stellar and gaseous distributions, and be more susceptible to a burst mode of star formation.

Subject headings: galaxies: compact — galaxies: dwarf — galaxies: evolution — galaxies: individual (UM 38, UM 323, MK 1418, MK 750, MK 900, MK 324) — galaxies: kinematics and dynamics

1. INTRODUCTION

Blue compact dwarf (BCD) galaxies pose an interesting puzzle for standard galaxy evolution models. Their extremely low gas-phase metallicities and blue colors suggest that these galaxies are relatively unevolved systems, perhaps undergoing their first bursts of star formation at the present epoch (e.g., Sargent & Searle 1970; Izotov & Thuan 1999; Thuan et al. 1999). Recently, however, deep optical and infrared imaging of BCDs have shown that the majority have extensive low surface brightness stellar halos, indicating that most have an underlying older stellar population in addition to bright young stars from the present starburst (e.g., James 1994; Papaderos et al. 1996a,b). Thus, despite their low luminosity, low metallicity nature, most BCDs are not young systems; rather, the burst phase in BCDs is a transitory event, and perhaps cyclical in nature.

This immediately raises the question: where are the quiescent-phase BCDs today? Are they included as part of the large, diverse, class of dwarf irregulars? Do BCDs use up their gas and fade into dwarf ellipticals? Or, do they fade beyond detectability, and thus lie hidden and ignored in the vastness of space? The possibility of morphological evolution among the dwarf galaxy classifications (dE, dI, BCD, in order of increasing star formation activity) has been suggested many times over the last several decades (e.g., Loose & Thuan 1986; Silk et al. 1987; Davies & Phillipps 1988; Hoffman et al. 1989; Drinkwater & Hardy 1991; James 1994; Ferguson & Binggeli 1994; Papaderos et al. 1996a), with a long list of positive and negative attributes for each of the various possible transformations. One of the popular evolutionary scenarios is that the starburst phase uses up (or “blows-out,” Dekel & Silk 1986) the interstellar medium. As the young stars fade, the system will then evolve into a gas-poor, red, dwarf elliptical.

Alternatively, if the gas is not entirely consumed, the system could continue to form stars at a much lower rate, and thus be classified as a gas-rich dwarf irregular.

The possibility of evolutionary connections between BCDs, dIs, and dEs has largely been based on the remarkable similarity in their stellar distributions. While exceptions exist, the majority of these low mass objects are well-fit by exponential disks; furthermore, in a plot of magnitude vs. surface brightness, the dE class is distinct from the giant elliptical class, but overlaps with the dIs (e.g., Ferguson & Binggeli 1994). The similarity in stellar distributions (but not current stellar populations or gas content) suggested that dEs could be faded dIs, or in some cases, such as the nucleated dwarf ellipticals, faded BCDs.

Recently, detailed kinematic studies of BCDs, dEs, and dIs has shed new light on the interrelationship between these low mass galaxies. High resolution HI kinematic studies of a number of BCDs indicate that these are rotation dominated systems (e.g., Walter et al. 1997; van Zee et al. 1998a,b). In contrast, stellar kinematic observations of dEs find little to no evidence of rotational support (Bender & Nieto 1990; Bender et al. 1991); if the gas and stars are kinematically coupled in BCDs, these results suggest that BCDs cannot evolve into dEs because of angular momentum conservation considerations. However, the BCD classification covers a large range of morphological types of “host” galaxies (e.g., Loose & Thuan 1985), and the previous samples did not include systems that were necessarily likely to evolve into dEs. Thus, finding rotation in those BCDs does not preclude this scenario for all types of BCDs. In order to test directly the feasibility of the popular BCD to dE evolutionary scenario, we have obtained HI synthesis observations of a small sample of BCDs which appeared to be “hosted” by dwarf elliptical-like systems; that is, this sample contains the systems that are *most likely* to be morphologically similar to dEs when their starburst fades.

In this paper, we present the results of high spatial resolution HI synthesis observations of six BCDs. We discuss the sample selection and observational procedures in Section 2. The HI distributions and kinematics of the six galaxies are presented in Section 3. A discussion of the neutral gas dynamics and its implications for BCD evolutionary scenarios is presented in Section 4; Section 5 contains a brief summary of the conclusions.

2. DATA ACQUISITION AND ANALYSIS

Multiconfiguration HI observations of six BCDs were obtained with the Very Large Array¹. In this section, the sample selection and procedures for observation and data reduction are discussed.

2.1. Sample Selection

The BCD classification covers a large range of morphological types of “host” galaxies. Within the BCD class, there are a handful of galaxies which appear to be hosted by dwarf ellipticals; that is, aside from the central starburst, the underlying stellar distribution has smooth, elliptical isophotes. These BCD/dEs are the *most likely* subclass of BCDs to look like dEs after the starburst fades.

We thus selected a small sample of BCD/dEs in order to investigate their gas kinematics and distributions. The galaxies in the present sample were selected from a large HI survey of blue compact dwarf galaxies (Salzer et al. 2001).

Physical properties of the selected galaxies are summarized in Table 1. The distance to each system was calculated from the systemic velocity using a Virgocentric infall model based on the outline of Schechter (1980) and an H_0 of $75 \text{ km s}^{-1} \text{ Mpc}^{-1}$. Optical diameters and luminosities were taken from the tabulation of Salzer et al. (2001). The absolute blue magnitudes have been corrected for Galactic extinction, but not for internal extinction or for nebular contributions to the broadband luminosity. All six galaxies are at comparable distances and have similar luminosities. Their oxygen abundances, however, span a wide range (Terlevich et al. 1991; Izotov & Thuan 1999; Salzer, private communication). The L-band continuum flux listed in Table 1 was measured from the line-free channels of the HI observations (see Section 2.2); while the HI observations were not optimized for continuum detection, weak 20-cm continuum emission was found associated with all six BCDs.

2.2. HI Imaging Observations

Observations of UM 38, UM 323, MK 1418, MK 750, MK 900, and MK 324 were obtained with the VLA in its B and CS configurations during 1998–2000. As currently implemented, the CS configuration is a modified version of the C configuration where a telescope from the middle of the north arm is re-positioned at an inner D configuration station to provide improved coverage of the short spacings. A summary of the observing sessions and the total on-source integration times are listed in Table 2. During all observing sessions, the correlator was used in 2AD mode with the right and left circular polarizations tuned to the same frequency; the total bandwidth was 1.56 MHz. The on-line Hanning smoothing option was selected, producing final spectral data cubes of 127 channels, each 2.6 km s^{-1} wide. Standard tasks in AIPS (Napier, Thompson, & Ekers 1983) were employed for calibration and preliminary data reduction. Each set of observations was calibrated separately, using 3C 48 or 3C 286 as the flux and bandpass calibrator and nearby continuum sources as phase calibrators. For all except MK 324, continuum emission was removed with the AIPS task UVLIN after the combination of $u-v$ data sets and prior to transformation to the $x-y$ plane.

The line data were transformed to the image plane with several weighting schemes and combinations of configurations. To check the data quality, maps were made for each observing session. The data cubes presented in this paper were made from the combined data sets of the B and CS configuration observations. A robust weighting technique was employed by the AIPS task IMAGR to optimize the beam shape and noise levels (Briggs 1995). The “robustness parameter” in IMAGR controls the weighting of the $u-v$ data, permitting a fine-tuning between sensitivity and resolution in the final data cubes. As currently implemented, a robustness of 5 corresponds to natural weight-

¹The Very Large Array is a facility of the National Radio Astronomy Observatory. The National Radio Astronomy Observatory is a facility of the National Science Foundation, operated under a cooperative agreement by Associated Universities Inc.

ing of the $u-v$ data (maximizing sensitivity at the cost of spatial resolution) while a robustness of -5 corresponds to uniform weighting (maximal spatial resolution with lower sensitivity). Additionally, some maps were made with $u-v$ tapers to increase their sensitivity to low column density material. The relevant IMAGR parameters for a selected sample of the maps are listed in Table 3. Throughout this paper we will refer to the lowest resolution, tapered data cubes as the “tapered cubes”, to the robustness of 5 cubes as the “natural weight cubes”, and to the robustness of 0.5 cubes as the “intermediate weight cubes.” All subsequent analysis was performed within the GIPSY package (van der Hulst et al. 1992).

The reduction stream for the MK 324 observations differed slightly from the above synopsis. First, line emission from MK 324 and EXG 2323+1816 filled much of the bandpass, making it impossible to remove the continuum emission in the $u-v$ plane. A continuum image was created for each data cube by averaging the few line-free channels; this image was then subtracted from the original data cube. Second, due to the low signal-to-noise of the line emission in MK 324, the data were smoothed during the transformation to the $x-y$ plane by averaging 2 consecutive channels, resulting in a cube of 63 channels, each 5.2 km s^{-1} wide.

To determine if the total flux density was recovered in the HI synthesis observations, total integrated profiles were constructed from the natural weight data cubes after correcting for the primary beam shape with the GIPSY task PBCORR (Figure 1). For all systems, the total flux density recovered in the VLA maps is in good agreement (within 10%) with previous single dish flux measurements (e.g., Huchtmeier & Richter 1986; van Zee et al. 1995; Salzer et al. 2001). The total HI masses listed in Table 1 were calculated from the observed VLA flux density and the assumed distance to the system.

Moment maps of each data cube were computed in the following manner. For each galaxy, both the tapered and natural weight cubes were smoothed to a resolution of twice the beam; the smoothed cubes were clipped at the 2σ level; the resultant clipped cubes were then interactively blanked to remove spurious noise spikes. Signal was identified based on spatial continuity between channels. A conditional transfer was used to blank the corresponding locations in both of the original data cubes, and in the intermediate weight data cube, after correcting for primary beam attenuation. Moment maps of the tapered, natural, and intermediate weight data cubes were created with the GIPSY task MOMENTS and are presented in Figures 2–7.

In the process of making moment maps, each data cube was searched for possible companion galaxies. Nearby systems were identified in the lowest resolution data cubes of both UM 323 and MK 324 (Figures 8 and 9); we designate these objects as EXG 0123-0040 and EXG 2323+1816, respectively. Both EXG 0123-0040 and EXG 2323+1816 have good positional coincidences with faint optical galaxies. Other HI synthesis observations of UM 323 also identified an HI signal near the location of EXG 0123-0040 and at a similar velocity, designated as UM 323A (Taylor et al. 1995); while this original detection was subsequently

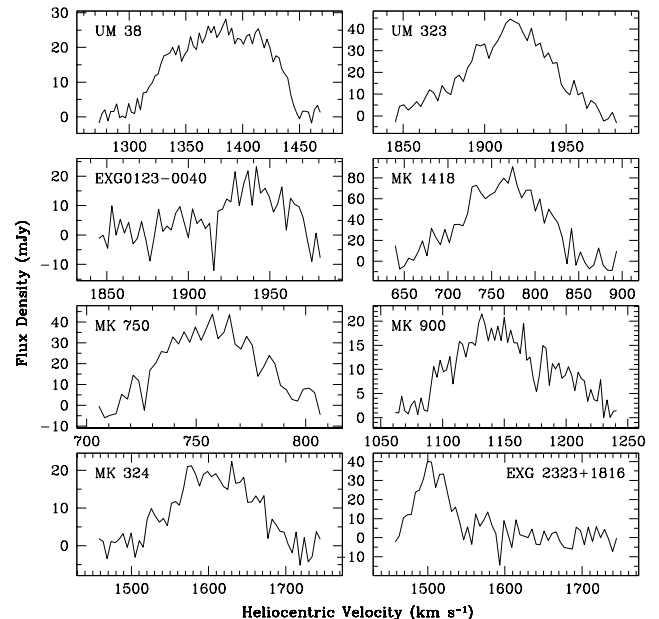


FIG. 1.— Integrated HI profiles of the BCD sample and of the two dwarf galaxies serendipitously discovered within the VLA primary beams.

retracted (see Taylor et al. 1996), this is probably the same object. Note that the present data set is completely independent from the previous D configuration observations of Taylor et al. (1995). The integrated HI profiles of these systems are shown in Figure 1; the observed HI flux densities, systemic velocities, and velocity widths are tabulated in Table 4. The primary beam correction may underestimate the total HI flux density of these systems since both of these galaxies are located slightly beyond the half power point of the main beam (see D_{center} in Table 4). Both systems are at a projected distance of ~ 130 kpc from the BCD, and have similar HI masses (30% and 70% of the target galaxy, respectively). These systems may not be either sufficiently massive, or close enough, to have “triggered” the current burst of star formation in UM 323 and MK 324, but the continuing detection of faint, but gas-rich, systems which have been missed by optical surveys (e.g., Wilcots, Lehman, & Miller 1996; Walter et al. 1997; Pisano & Wilcots 1999) suggests that HI observations are a crucial step in the process of determining the local environment of a galaxy.

2.3. Optical Imaging

Complementary optical images were obtained during several observing runs at KPNO.² $H\alpha$ and B-band images of UM 323, MK 750, MK 900, and MK 324 were obtained in 1989–1990 with the KPNO No. 1 0.9m telescope; the observation and data reduction procedures for these images were similar to those described in Salzer et al. (1991). $H\alpha$ and B-band images of UM 38, MK 900, and MK 324 were obtained with the KPNO 0.9m telescope in June 1998; the observation and reduction procedures for these images are described in van Zee (2000). Since no optical images were available for MK 1418, or for the extended fields around UM 323 and MK 324, images of these

²Kitt Peak National Observatory is part of the National Optical Astronomy Observatories that are operated by the Association of Universities for Research in Astronomy, Inc. under contract to the National Science Foundation.

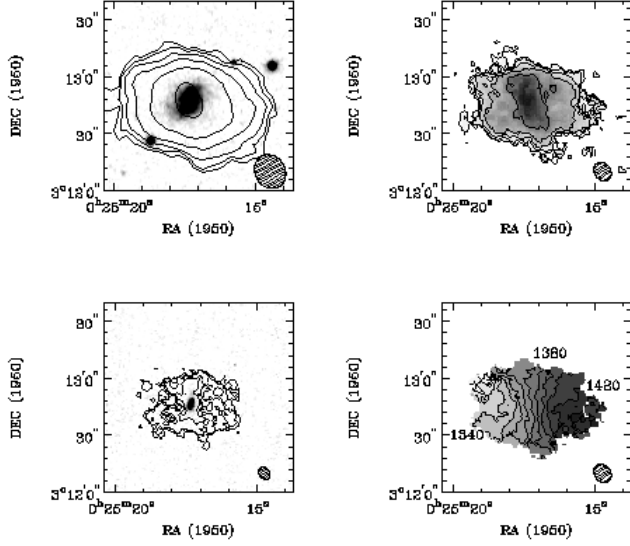


FIG. 2.— Moment maps of UM 38. (a) The HI contours from the tapered data cube are shown overlaid on a B band image. The HI contours are $0.5, 1, 2, 4, 8,$ and 16×10^{20} atoms cm^{-2} with a beam size of 18.5×15.8 arcsec. The pixel scale of the optical image is 0.688 arcsec pixel^{-1} . (b) The integrated intensity map from the natural weight data cube. The HI contours are $1, 2, 4, 8,$ and 16×10^{20} atoms cm^{-2} . The beam size is 10.4×8.4 arcsec. (c) The HI contours from the intermediate weight data cube overlaid on an H α image. The HI contours are $0.4, 0.8,$ and 1.6×10^{21} atoms cm^{-2} with a beam size of 7.0×5.4 arcsec. The pixel scale of the H α image is 0.688 arcsec pixel^{-1} . (d) The velocity field from the natural weight data cube. The contours are marked every 10 km s^{-1} .

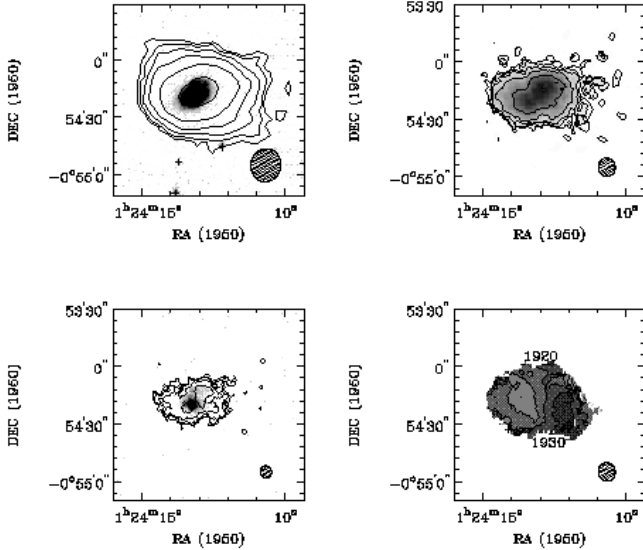


FIG. 3.— Moment maps of UM 323. (a) The HI contours from the tapered data cube are shown overlaid on a B band image. The HI contours are $0.5, 1, 2, 4, 8,$ and 16×10^{20} atoms cm^{-2} with a beam size of 17.4×15.6 arcsec. The pixel scale of the optical image is 0.43 arcsec pixel^{-1} . (b) The integrated intensity map from the natural weight data cube. The HI contours are $1, 2, 4, 8,$ and 16×10^{20} atoms cm^{-2} . The beam size is 9.6×8.8 arcsec. (c) The HI contours from the intermediate weight data cube overlaid on an H α image. The HI contours are $0.3, 0.6, 1.2,$ and 2.4×10^{21} atoms cm^{-2} with a beam size of 6.5×6.0 arcsec. The pixel scale of the H α image is 0.43 arcsec pixel^{-1} . (d) The velocity field from the natural weight data cube. The contours are marked every 10 km s^{-1} .

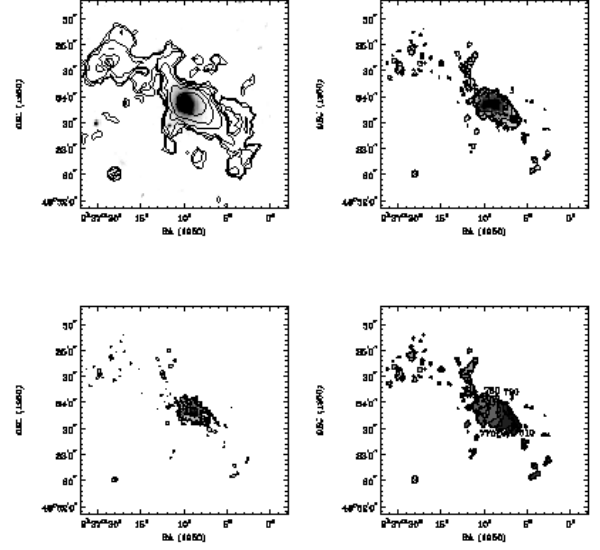


FIG. 4.— Moment maps of MK 1418. (a) The HI contours from the tapered data cube are shown overlaid on an optical image from the Digitized Sky Survey. The HI contours are $0.5, 1, 2, 4, 8,$ and 16×10^{20} atoms cm^{-2} with a beam size of 15.7×15.2 arcsec. The pixel scale of the optical image is 1.008 arcsec pixel^{-1} . (b) The integrated intensity map from the natural weight data cube. The HI contours are $1, 2, 4, 8,$ and 16×10^{20} atoms cm^{-2} . The beam size is 7.9×7.6 arcsec. (c) The integrated intensity map from the intermediate weight cube. The HI contours are $0.3, 0.6, 1.2,$ and 2.4×10^{21} atoms cm^{-2} with a beam size of 5.6×5.5 arcsec. (d) The velocity field from the natural weight data cube. The contours are marked every 10 km s^{-1} .

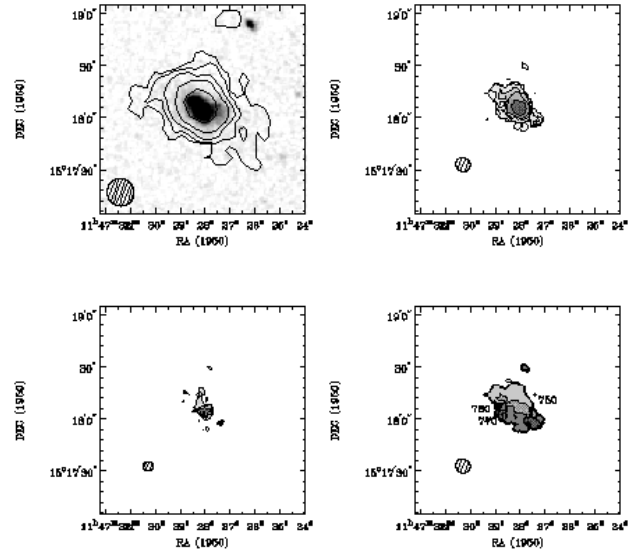


FIG. 5.— Moment maps of MK 750. (a) The HI contours from the tapered data cube are shown overlaid on a B band image. The HI contours are $0.5, 1, 2, 4, 8,$ and 16×10^{20} atoms cm^{-2} with a beam size of 16.1×15.5 arcsec. The pixel scale of the optical image is 1.008 arcsec pixel^{-1} . (b) The integrated intensity map from the natural weight data cube. The HI contours are $1, 2, 4, 8,$ and 16×10^{20} atoms cm^{-2} . The beam size is 8.7×7.7 arcsec. (c) The integrated intensity map from the intermediate weight cube overlaid on an H α image. The HI contours are $0.3, 0.6, 1.2,$ and 2.4×10^{21} atoms cm^{-2} with a beam size of 6.0×5.4 arcsec. The pixel scale of the H α image is 0.43 arcsec pixel^{-1} . (d) The velocity field from the natural weight data cube. The contours are marked every 10 km s^{-1} .

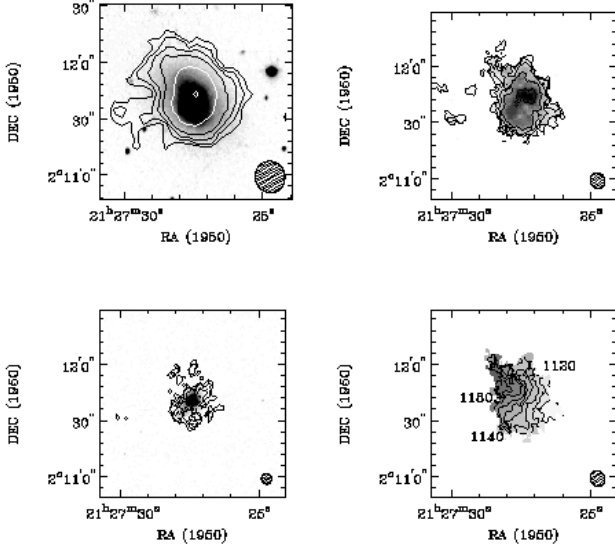


FIG. 6.— Moment maps of MK 900. (a) The HI contours from the tapered data cube are shown overlaid on an B band image. The HI contours are $0.5, 1, 2, 4, 8,$ and 16×10^{20} atoms cm^{-2} with a beam size of 17.0×15.9 arcsec. The pixel scale of the optical image is 0.688 arcsec pixel^{-1} . (b) The integrated intensity map from the natural weight data cube. The HI contours are $1, 2, 4, 8,$ and 16×10^{20} atoms cm^{-2} . The beam size is 8.6×7.8 arcsec. (c) The HI contours from the intermediate weight data cube overlaid on an H α image. The HI contours are $0.3, 0.6, 1.2,$ and 2.4×10^{21} atoms cm^{-2} with a beam size of 5.9×5.4 arcsec. The pixel scale of the H α image is 0.688 arcsec pixel^{-1} . (d) The velocity field of the natural weight data cube. The contours are marked every 10 km s^{-1} .

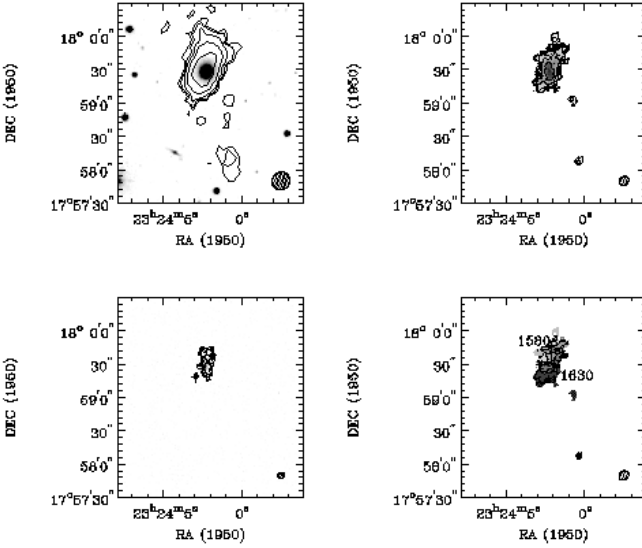


FIG. 7.— Moment maps of MK 324. (a) The HI contours from the tapered data cube are shown overlaid on a B band image. The HI contours are $0.5, 1, 2, 4, 8,$ and 16×10^{20} atoms cm^{-2} with a beam size of 16.7×15.7 arcsec. The pixel scale of the optical image is 0.688 arcsec pixel^{-1} . (b) The integrated intensity map from the natural weight data cube. The HI contours are $1, 2, 4, 8,$ and 16×10^{20} atoms cm^{-2} . The beam size is 9.4×7.7 arcsec. (c) The HI contours from the intermediate weight data cube overlaid on an H α image. The HI contours are $0.4, 0.8,$ and 1.6×10^{21} atoms cm^{-2} with a beam size of 6.1×5.2 arcsec. The pixel scale of the H α image is 0.688 arcsec pixel^{-1} . (d) The velocity field of the natural weight data cube. The contours are marked every 10 km s^{-1} .

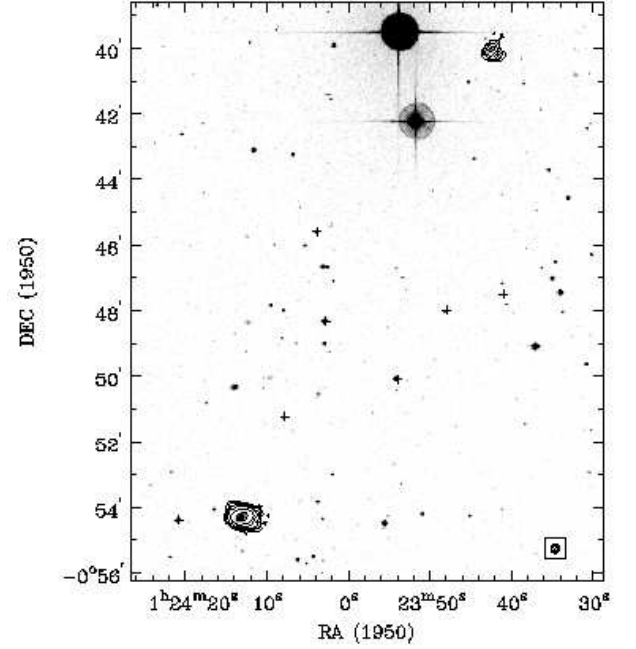


FIG. 8.— The HI contours from the tapered data cube are shown overlaid on an image from the Digitized Sky Survey for UM 323 and EXG 0123-0040. HI image has been corrected for primary beam attenuation. The HI contours are $0.5, 1, 2, 4, 8,$ and 16×10^{20} atoms cm^{-2} with a beam size of 17.4×15.6 arcsec.

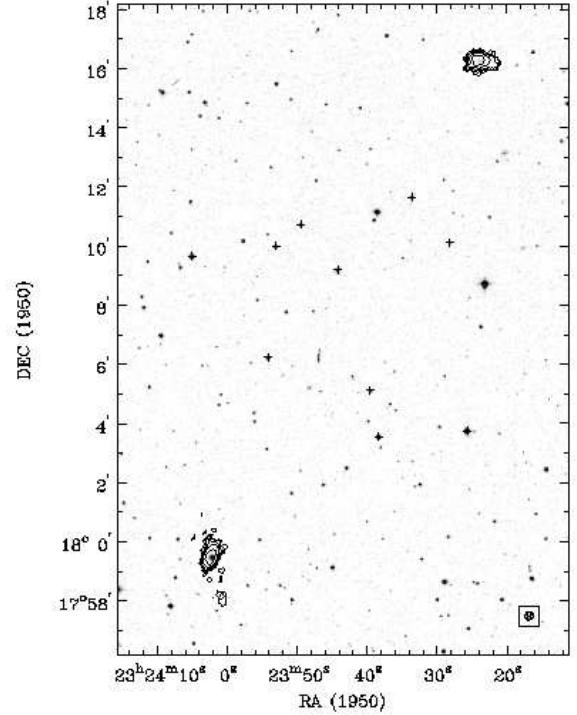


FIG. 9.— HI contours from the tapered data cube are shown overlaid on an image from the Digitized Sky Survey for MK 324 and EXG 2323+1816. The HI image has been corrected for primary beam attenuation. The HI contours are $0.5, 1, 2, 4, 8,$ and 16×10^{20} atoms cm^{-2} with a beam size of 16.7×15.7 arcsec.

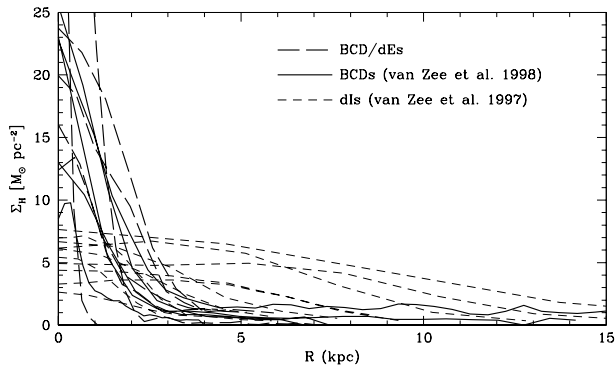


FIG. 10.— Azimuthal averages of the neutral gas distribution of BCDs (van Zee et al. 1998a) and dIs (van Zee et al. 1997). The gas distribution is more centrally concentrated in BCDs than in dIs.

fields were extracted from the Digitized Sky Survey³. Plate solutions for the optical images were derived from coordinates of at least five stars listed in the APM catalog⁴ and are accurate to $0.5''$.

Star formation rates were calculated from the $H\alpha$ images of UM 38, UM 323, MK 750, MK 900, and MK 324. First, the observed $H\alpha$ flux was corrected for internal and external absorption based on the observed spectroscopic Balmer line ratios (Terlevich et al. 1991; Salzer, private communication). The derived $H\alpha$ luminosity was then converted to the current star-formation rate (SFR), using the conversion factor from Kennicutt (1998):

$$\text{SFR} = 7.9 \times 10^{-42} L(H\alpha) M_{\odot} \text{ yr}^{-1}. \quad (1)$$

The current SFR and the gas depletion time scale (M_{HI}/SFR) are tabulated in Table 1. In general, the current SFRs of the BCDs are quite high, with typical gas depletion times of approximately 1-5 Gyr. However, it is important to note that the star formation rate conversion factor used here may lead to an overestimate of the star formation rate in low metallicity galaxies, since the UV opacity will be lower in metal-poor stars. Thus, it is possible that the gas depletion time scales quoted here are underestimates.

3. RESULTS OF HI SYNTHESIS IMAGING

3.1. HI Morphology

The neutral gas distributions of the six BCDs are shown in Figures 2–7. As has been seen in other observations of BCDs (e.g., Taylor et al. 1994; Meurer et al. 1996; Walter et al. 1997; van Zee et al. 1998b,a; Putman et al. 1998), the HI distribution extends well beyond the optical system. The HI-to-optical diameters (measured at the 10^{20} atoms cm^{-2} and 25 mag arcsec^{-2} isophotes, respectively) are tabulated in Table 1. For all except MK 900, the neutral gas extends approximately 2 times the optical diameter, which is quite typical for gas-rich galaxies (see, e.g., Broeils & van Woerden 1994; Broeils & Rhee 1997). Both MK 1418 and MK 324 have extended gaseous distributions which show kinematic peculiarities, reminiscent of tidal tails. Optically, these galaxies have smooth, regular isophotes, so it is not clear if they are merger remnants, recently had an interaction, or if some other mechanism produced their extended gaseous disks.

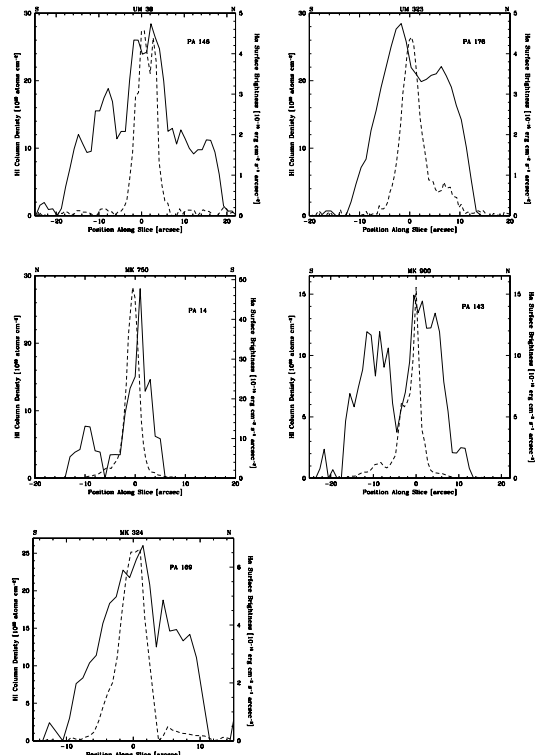


FIG. 11.— Comparison of the neutral (solid lines) and ionized gas (dashed lines) distributions in BCDs. In general, star forming regions are correlated with local peaks in the HI surface density. However, in several cases, such as UM 38, the star forming region appears to lie in a modest depression of the neutral gas, suggesting that star formation has had an impact on the neutral medium.

Overall, the neutral gas distribution in these BCD/dEs is quite similar to that found in other BCDs. Azimuthal averages of the gas distributions are shown in Figure 10 for the present sample, a random sample of BCDs (van Zee et al. 1998a), and a sample of gas-rich dIs (van Zee et al. 1997b). The gas is much more centrally concentrated in the BCDs [see also Taylor et al. (1994) and Simpson & Gottesman (2000)], which presumably facilitates their high star formation rates.

More specifically, the neutral gas is concentrated in the regions of star formation activity. Slices through the neutral and ionized gas images of UM 38, UM 323, MK 750, MK 900, and MK 324 are shown in Figure 11. The position angle of each slice was chosen so that the slice would intersect the brightest HII regions in each galaxy. As was seen with other BCDs (van Zee et al. 1998a), the neutral gas density peaks coincide with regions of star formation. However, in the highest spatial resolution observations there is some evidence of feedback between the star forming regions and the neutral medium. For instance, the brightest HII region in UM 38 is actually located in a slight depression in the neutral gas surface density, as would be expected if the neutral medium has been partially used, or ionized, by the star formation activity.

The observed peak column densities are tabulated in Table 5. Since the observed column density depends on the beam dilution, the value determined in each data cube is

³The Digitized Sky Surveys were produced at the Space Telescope Science Institute under U.S. Government grant NAG W-2166.

⁴<http://www.ast.cam.ac.uk/~apmcat/>

presented. In general, the observed peak column densities are between $2\text{--}4 \times 10^{21}$ atoms cm^{-2} ; when corrected for inclination and neutral helium content, the peak neutral gas surface densities are on the order of 3×10^{21} atoms cm^{-2} for all six galaxies. Interestingly, these peak values are very similar to the predicted critical density as calculated from the Toomre (1964) instability criterion (e.g., Kennicutt 1989).

3.2. Neutral Gas Kinematics

3.2.1. Velocity Fields

The velocity fields are shown in Figures 2d–7d. In all cases, a clear velocity gradient is present; interestingly, the velocity gradient is aligned along the optical major axis of only MK 900 and MK 324. Both UM 38 and MK 900 have relatively smooth, ordered velocity fields while those for UM 323, MK 1418, MK 750 and MK 324 are significantly more complicated. Less than perfect ordered rotation has also been found in other high spatial resolution observations of BCDs (e.g., van Zee et al. 1998b,a). Nonetheless, despite the kinematic complexities, it is clear that these systems all have large rotation velocities.

3.2.2. Rotation Curves

Model rotation curves for the BCDs were derived from tilted-ring analysis of the observed velocity fields using the GIPSY task ROTCUR. The process of fitting a rotation curve is iterative. First, the kinematic center and systemic velocity were determined using both sides of the velocity field to constrain these global parameters. Next, the center and systemic velocity were held fixed while the inclination angle and position angle were derived. Unfortunately, the complex nature of the velocity fields imply a large degree of uncertainty in the kinematic parameters; for all except UM 38, the derived kinematic parameters (Table 6) should only be considered rough estimates. In particular, it was not possible to constrain the inclination angle based on the velocity field alone; an estimate of the inclination angle was derived from the observed axial ratios (both HI and optical). Finally, despite the apparent solid body nature of the velocity fields, the final rotation curves produced by ROTCUR had a tendency to flatten in the outer parts; thus, in the end, only UM 38 was satisfactorily fit by this method.

Nonetheless, the ROTCUR fits were sufficient to indicate the major axis of each galaxy so that position-velocity diagrams could be created (Figure 12). As expected from the velocity fields, the p–v diagrams indicate solid body rotation throughout the gas disk for UM 323, MK 1418, MK 750, MK 900, and MK 324, while UM 38 appears to be differentially rotating in the outer disk. Also shown in Figure 12 is the expected observed rotation curve from the ROTCUR model for UM 38, and estimates of solid body rotation curves for the other galaxies. In fact, the p–v diagrams provide a good estimate of the rotation curves for UM 323, MK 1418, MK 750, MK 900, and MK 324, assuming that no warps or other kinematic abnormalities are present. This is probably a reasonable assumption for MK 900, but the derived kinematic parameters for the other four galaxies are significantly more uncertain.

The radii and velocities (corrected for inclination) of the last measured points of the rotation curves are tabulated

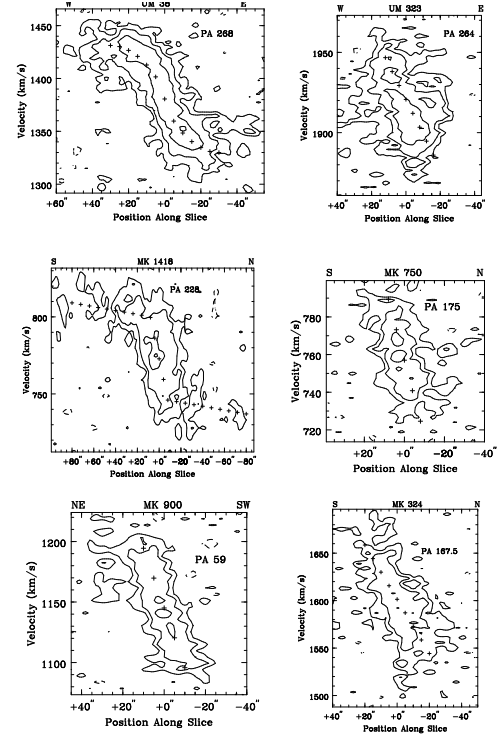


FIG. 12.— Position–Velocity diagrams from the natural weight data cubes; the UM 38 and MK 900 data cubes have been hanning smoothed. The contours represent -3σ , 3σ , 6σ , and 12σ . A rotation curve as derived from tilted-ring models is superposed on the p–v diagram for UM 38; in the other five panels, crosses denote the adopted solid body rotation curves.

in Table 6. Since the rotation curves were poorly constrained for all except UM 38 and MK 900, these values are only rough estimates. If the BCDs are dark matter dominated, as has been found for virtually all dwarf galaxies studied (e.g., Carignan & Beaulieu 1989), the dynamical mass can be calculated from the derived rotation curves. For a spherical mass distribution (appropriate for most dark matter halos), the dynamical mass within radius r is:

$$M_T(r) = 2.326 \times 10^5 V^2(r) r \quad (2)$$

where $V(r)$ is in km s^{-1} and r is in kpc. The derived dynamical masses for the last measured point of the rotation curves are tabulated in Table 6. The HI-to-dynamical mass ratios for UM 38, MK 1418, MK 750 and MK 900 are quite typical for dwarf galaxies in general (e.g., Skillman et al. 1987; van Zee et al. 1997b) while those of UM 323 and MK 324 are significantly higher than average. However, both UM 323 and MK 324 had extremely complex velocity fields, so this may simply reflect on the poorly derived rotation curves, rather than an intrinsic difference in galaxy properties.

3.2.3. Thermal Motions

An estimate of the neutral gas velocity dispersion was obtained from Gaussian fits to the spectral profiles in the natural weight data cubes. The median σ is tabulated in Table 6. The observed velocity dispersions are quite typical of dwarf galaxies (e.g., Young & Lo 1996; van Zee et al. 1997b). In all cases, the observed velocity dispersions are significantly less than the rotational component in these

galaxies, indicating that these systems are rotation dominated.

4. DISCUSSION

4.1. The Dynamics of BCDs

Based on these and other observations of BCDs and dIs (e.g., van Zee et al. 1997b, 1998a; Swaters 1999), it appears that all types of moderate luminosity gas-rich dwarf galaxies are rotation dominated systems. In particular, as illustrated in Figure 12, the BCD/dEs show significant velocity gradients across the optical and HI disks, which implies that the gaseous disks have significant angular momenta. The specific angular momenta for a given radius in the disk can be calculated from the derived rotation curves:

$$J/M = V \times R \quad (3)$$

where J/M is the specific angular momenta, V is the rotation velocity, and R is the radius. It is difficult to specify a “characteristic” value for the specific angular momentum of the disk in low mass galaxies because the specific angular momentum increases with radius for galaxies undergoing solid-body rotation. However, it is useful to compare the specific angular momenta of the outermost neutral hydrogen gas in BCDs and low surface brightness (LSB) dIs. The specific angular momenta of the extended HI disks were computed from the maximum rotation velocities and radii tabulated in Table 6 (BCDs) and in Table 4 of van Zee et al. (1997b) (LSBDGs). While the definition of “the outermost” gas is sensitivity dependent, the two studies shown in Figure 13 have similar sensitivities, and the galaxies have similar HI-to-optical ratios. As illustrated in Figure 13a, the BCDs have lower specific angular momenta than the LSB dIs, as one would expect for rotation curves which reach similar maximum velocities at smaller radii (Figure 13b). Since the rotation curves of dwarf galaxies are primarily solid body, the fact that BCDs reach a similar maximum velocity within a smaller radius implies that BCDs have steeply rising rotation curves.

The fact that BCDs appear to have steeply rising rotation curves (low angular momenta) has several interesting consequences for evolutionary studies of BCDs. First, the shape of the rotation curve suggests that the matter distribution is centrally concentrated (see also Meurer et al. 1998). As expected for galaxies which are classified as “compact,” studies of their stellar distributions indicate that the stars are centrally concentrated in BCDs (Salzer & Norton 1999; Norton & Salzer, in prep); similar results are found for the gaseous distribution as well (Figure 10). However, the rotation curve results also suggest that the dark matter distributions may be centrally concentrated in BCDs. Given the poor constraints on the derived rotation curves in this sample, we have elected to forgo extensive analysis at this time (i.e., dark matter decompositions). However, more extensive analysis could place strong constraints on dark matter models, since dwarf galaxies are usually dark matter dominated. BCDs clearly inhabit an important, and as yet unexplored, region of parameter space.

A second major implication from the observed rotation curve shapes (angular momenta) is that BCDs have higher threshold densities for the onset of star formation. Using the classic Toomre (1964) instability analysis for a rotating

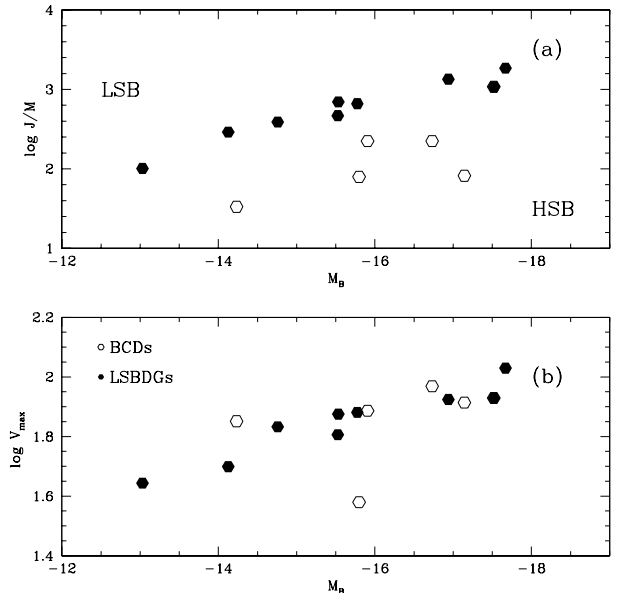


FIG. 13.— (a) Specific angular momenta of the outer gas disks in BCDs (open circles) and LSB dIs (filled circles, van Zee et al. 1997). The BCDs have lower specific angular momenta compared to comparable luminosity LSB dIs. (b) Maximum rotation velocities of the BCD and dI samples. Both types of galaxies have similar rotation velocities. The fact that both BCDs and LSB dIs follow the same luminosity–linewidth relation has implications for galaxy evolution models: BCDs have steeper rotation curves than the LSB dwarfs, and thus have lower angular momenta and higher critical densities for star formation.

disk, the threshold density for star formation can be derived from the balance between gravitational collapse and the effects of both thermal pressure and rotational shear. For a solid body rotation curve, this type of analysis results in a star formation threshold density which is proportional to the slope of the rotation curve. In other words, a galaxy with a steep rotation curve (low specific angular momenta) will have a higher threshold density for star formation. While the instability threshold is a global dynamical property, it is particularly important to note that the current observed gas column densities appear to hover around the instability threshold densities in both the BCDs (this paper and van Zee et al. 1998a) and dIs (van Zee et al. 1997b), and that the local column density peaks are correlated with sites of current star formation activity. Thus, there appears to be a strong connection between crossing the global instability threshold and the onset of star formation, a local process.

Angular momentum appears to play a crucial role in determining the ultimate star formation history of a low mass galaxy. The gas associated with a galaxy with high angular momentum will have difficulty collapsing, and thus at the present day it will appear as a diffuse, low surface brightness galaxy. On the other hand, the gas associated with galaxies with low angular momenta will be able to collapse further, leading to smaller, compact, high surface brightness galaxies. Concurrently, in these compact systems, the onset of star formation may be delayed because the threshold density is extremely high. For example, if the infalling gas accretes at a steady rate, it will take longer for the gas density to exceed the critical density in a galaxy with lower angular momenta. Further, once the gas density does exceed the critical density, there will be a large fuel supply

readily available for star formation. It is thus quite likely that these low angular momenta, high density systems will be more susceptible to a “burst” mode of star formation than similar mass, but high angular momenta, low density systems. It is also logical to hypothesize that starbursts will occur episodically in these compact systems, with the starburst duty cycle regulated by the frequency at which the central gas density reaches the critical density for star formation.

4.2. Dwarf Galaxy Evolutionary Scenarios

As mentioned in the introduction, one of the key questions in dwarf galaxy evolution is the ultimate fate of the star-bursting dwarf galaxies. Since the starburst phase in BCDs is expected to be a transitory event which lasts only a few 100 Myr, one logical hypothesis is that BCDs must evolve from (and into) other types of low mass galaxies. Several of the major unresolved issues in dwarf galaxy evolutionary scenarios are: (1) do all dwarf galaxies undergo a starburst phase? (2) what mechanisms initiate or trigger a starburst event? (3) what mechanisms terminate a starburst event? and (4) how does the galaxy evolve after the burst phase?

For the last 30 years, most discussions of dwarf galaxy evolutionary scenarios have centered around the morphological similarities between starbursting dwarf galaxies, dwarf irregular galaxies, and dwarf elliptical galaxies (e.g., Lin & Faber 1983; Kormendy 1985; Loose & Thuan 1986; Drinkwater & Hardy 1991; James 1994; Papaderos et al. 1996a; Sung et al. 1998). These studies have shown that the stellar distributions of all three types of low mass galaxies are well fit by exponential profiles, with a few notable exceptions (e.g., Doublier et al. 1997, 1999). Thus, based on the stellar distributions alone, it has been argued that BCDs can evolve into either the dwarf elliptical class or dwarf irregular class with only minor changes in the stellar distribution and optical morphology. Arguments against such passive morphological evolution usually focus on the fact that the stellar distributions of BCDs are much more compact than the typical dwarf irregular or dwarf elliptical galaxy; however, since there is some overlap in the distribution functions for all three type of galaxies, such morphological evolution cannot be excluded based on the stellar distributions alone.

In the next two sections we outline the arguments for and against the canonical BCD evolutionary scenarios. First, in Section 4.2.1, we discuss whether gas-rich BCDs can evolve into gas-poor dwarf ellipticals. Second, in Section 4.2.2, we discuss whether post-burst BCDs can be found within the general population of gas-rich dwarf irregular galaxies. A similar discussion with a focus on the evolution of dwarf irregular galaxies may be found in Skillman & Bender (1995).

4.2.1. BCD to dE: Quenching the Burst

Secular evolution from BCD to dE requires more than just fading of the central starburst. All of the dwarf ellipticals in the Local Group are gas-poor (with $M_{\text{HI}} < 10^5 M_{\odot}$, Young & Lo 1997; Young 1999, 2000), while the BCDs are gas-rich systems, with $M_{\text{HI}} > 10^7 M_{\odot}$. Thus, evolution from BCD to dE requires either efficient gas consumption or removal of the remaining interstellar medium. The lat-

ter process can be accomplished in at least two distinct ways: (1) Dekel & Silk (1986) proposed that a starburst might have sufficient kinetic energy to disrupt the interstellar medium in a low mass galaxy, and (2) Lin & Faber (1983) proposed that the ISM might be removed via ram pressure stripping.

Hydrodynamic models initially indicated that a starburst could have a disastrous effect on the interstellar medium within a low mass galaxy (e.g., Dekel & Silk 1986; De Young & Gallagher 1990); however, recent models, which include a large dark matter component, have shown that it is much more difficult to remove the interstellar medium with a single starburst than previously thought (e.g., De Young & Heckman 1994; Silich & Tenorio-Tagle 1998; Mac Low & Ferrara 1999). Rather, while some of the hot, ionized gas may escape (as possibly seen in NGC 1569, Heckman et al. 1995), the neutral medium is largely unaffected by the starburst. Further, detailed star formation histories of the Local Group dEs indicate that these dwarf galaxies appear to have had several discrete star-formation episodes (Mateo 1998), rather than the single burst envisioned by Dekel & Silk (1986). Thus, it now appears that it is unlikely that a single starburst will completely use up, or blow-out, the interstellar medium of a dwarf galaxy.

Ram pressure stripping, on the other hand, is still a viable mechanism to remove the remnants of the ISM in a post-burst low mass galaxy. Ram pressure stripping will occur predominantly in high density regions, the exact type of environment favored by dwarf elliptical galaxies. However, this process will operate regardless of the star formation activity in the low mass galaxy; thus, while this is a viable mechanism to transform a gas-rich star forming galaxy into a gas-poor evolved galaxy, it is tangential at best to the main discussion of the evolutionary fate of star-bursting dwarf galaxies.

The neutral gas kinematics presented here and in van Zee et al. (1998a) provide the first definitive evidence that the majority of BCDs will not evolve passively into dwarf elliptical galaxies. All of the BCDs studied so far are rotation dominated and have significant angular momenta. In contrast, dwarf elliptical galaxies are not rotationally supported (Bender & Nieto 1990; Bender et al. 1991). Of the 5 dwarf ellipticals observed, only one has a maximum stellar rotation velocity $> 15 \text{ km s}^{-1}$; the remainder are consistent with zero stellar rotation. As mentioned previously, the BCDs in the present study were selected specifically to have optical properties similar to dwarf elliptical galaxies, since these would be the *most likely* to be classified as dwarf ellipticals after the starburst; however, even these galaxies have significant rotation velocities. Thus, these observations indicate that BCDs cannot evolve passively into dwarf elliptical galaxies since such a morphological evolution would require the loss of angular momentum.

Further, the possibility that ram pressure stripping may be a necessary process to remove the interstellar medium during the formation of dwarf elliptical galaxies leads directly to another strong argument against generic morphological evolution from a starbursting dwarf galaxy to a dwarf elliptical (such as the one envisioned by Dekel & Silk 1986): BCDs and dEs have very different clustering properties. Dwarf ellipticals are generally found in clus-

ters or as companions to massive galaxies while BCDs are typically field objects. In fact, dEs are among the most strongly clustered galaxies known (Ferguson & Sandage 1989), while BCDs are among the least clustered (Iovino et al. 1988; Rosenberg, Salzer, & Moody 1994; Pustil’nik et al. 1995; Lee et al. 2000). Thus, it may be necessary to consider the evolution of field and cluster dwarf galaxies separately: BCDs formed in the field will probably retain a substantial fraction of their ISM, even after the starburst phase, and thus will be classified as dwarf irregular galaxies if identified either pre- or post-burst; meanwhile, some BCDs formed in cluster environments may evolve into dwarf elliptical galaxies, but such morphological evolution will not occur via passive secular evolution.

4.2.2. BCD to dI: Quelling the Burst

One of the difficulties for discussions of BCD to dI evolutionary scenarios is a nomenclature issue: in many regards, BCDs *are* dIs. Since the dwarf irregular classification is usually based on irregular morphology and gas-richness, star-bursting dwarf galaxies are included in this more general classification. Thus, rather than true morphological evolution, the BCD to dI evolutionary scenario is a matter of degree: can post-burst BCDs be found within the general dwarf irregular class, and also, is a starburst phase common to all gas-rich low mass galaxies?

These questions have been addressed extensively by van Zee (2000, 2001), who argues that the majority of dIs do not go through a starburst phase. Rather, the star formation histories of most dwarf irregular galaxies are best described by a low level of star formation activity which percolates across the gaseous disk. However, large imaging studies of dwarf irregular galaxies have shown that there are a few dIs which have structural parameters similar to the BCD class (e.g., Patterson & Thuan 1996; van Zee 2000). These “compact dIs” have similarly small scale lengths for their luminosity, but do not have extremely high star formation rates at the present time. Thus, these galaxies are likely to be examples of post-burst BCDs. Indeed, unlike the other dwarf irregular galaxies in the samples, the “compact dIs” have detectable color gradients from the inner to outer regions of the stellar disk, similar to those found in samples of starbursting dwarf galaxies (e.g., Marlowe et al. 1995; Doublier et al. 1997, 1999).

The kinematic data presented here provides additional evidence that BCDs do not represent a common phase in the star formation history of gas-rich low mass galaxies. BCDs have steeper rotation curves and lower specific angular momenta than “typical” dwarf irregular galaxies (Figures 12 and 13, see also Meurer et al. 1998). However, this is not to say that there is no overlap between BCDs and dIs in this regard as well. In order to accentuate the differences between BCDs and dIs, we have focussed here on examples taken from the extremes of both populations (LSB and HSB). In fact, dIs embody a continua of properties, from the low surface brightness regime to the high surface brightness regime, and with a wide range of star formation rates and gas content. Thus, the marked differences seen in Figures 10 and 13 should not be used to infer that post-burst BCDs are morphologically and dynamically distinct from general dI classification. Instead, it appears that post-burst BCDs can be found within the

general dI classification, but rather than being a necessary phase in dwarf galaxy evolution, starbursting episodes are rare events.

4.3. Dwarf Galaxy Evolution and Cosmology

As the first structures to collapse in hierarchical galaxy formation models, dwarf galaxies play a crucial role in galaxy formation. However, the interplay between structure formation, the onset of star formation activity, and the subsequent evolution of baryonic matter is complex and not well understood at the present time. Most cosmological models treat the physics of the dark matter particles in great detail, while the complex processes of star formation and gas dynamics are applied as simplified “recipes” (e.g., White & Frenk 1991; Kauffmann, White, & Guiderdoni 1993; Cole et al. 1994; Heyl et al. 1995; Somerville & Primack 1999; Cole et al. 2000). Unfortunately, this broad brush approach to star formation means that all dwarf galaxies are treated in a similar manner, regardless of their physical attributes; further, none of the current models have the spatial resolution to track the gas distribution in individual galaxies, and thus they cannot determine if a galaxy is likely to form stars in a large burst of star formation (centrally concentrated gas distributions), or in a more quiescent and constant manner (low density gas distributions). Ultimately, the lack of spatial resolution and the poor treatment star formation processes means that current cosmological models cannot differentiate between low surface brightness dwarf galaxies and high surface brightness dwarfs.

As discussed in Section 4.2.2, low surface brightness dwarf galaxies and high surface brightness (starbursting) dwarf galaxies probably represent the extreme ends of a continua of dwarf galaxy properties. One of the critical parameters which still needs to be determined is the relative number density of starbursting dwarf galaxies to quiescent dwarfs. In particular, BCDs have gained attention recently due to the identification of bursting systems at intermediate and high redshifts. Ferguson & Babul (1998) proposed that very intense and short bursts of star formation in low mass galaxies (similar to the present day BCDs) could be responsible for the faint blue galaxy excess found in studies of high redshift luminosity functions (e.g., Cowie, Songalia, & Hu 1991). However, if BCDs represent the extreme members of the dwarf irregular class, and occur only rarely, then only a small fraction of dwarf galaxies will go through a starburst phase. As a consequence, the number density of starbursting dwarf galaxies as a function of redshift may be lower than previously thought.

The possibility that there may be fewer starbursting dwarf galaxies at high redshift also has severe implications for galaxy evolution models. Most cosmological models assume that the net effect of any star formation activity in a dwarf galaxy is the immediate injection of heavy elements into the intergalactic medium via galactic winds and other “feedback” processes (e.g., Sommer-Larsen, Gelato, & Vedel 1999; Cole et al. 2000; Efstathiou 2000). These models predict rapid enrichment of the intergalactic medium, as low mass halos (dwarf galaxies) collapse in the early universe. If the majority of dwarf galaxies do not go through a starburst phase, however,

this enrichment process may be less efficient than currently assumed.

5. SUMMARY AND CONCLUSIONS

In summary, we have presented the results of high spatial resolution HI synthesis observations of six BCD/dEs. Our results and conclusions are summarized below.

(1) All six of the BCDs in this sample are rotation dominated systems. The velocity fields and position–velocity diagrams clearly indicate that these galaxies have significant velocity gradients across the gaseous disks (Figure 12).

(2) As in previous studies of BCDs (e.g., van Zee et al. 1998a), the neutral gas density is centrally concentrated (Figure 10), which presumably facilitates the high star formation rate in these compact galaxies.

(3) Starbursting dwarf galaxies appear to have lower specific angular momenta than similar luminosity low surface brightness dwarf irregular galaxies (Figure 13). The intrinsic angular momenta differences may explain both the compact nature of BCDs and their tendency to have starburst episodes.

(4) The observed gas dynamics places strong constraints on the evolutionary fate of starbursting dwarf galaxies. Based on their gas kinematics, BCDs cannot evolve passively into dwarf elliptical galaxies. In contrast, both BCDs and dIs are rotationally supported systems, and thus it is likely that post–burst BCDs can be found within the general dwarf irregular classification.

These observations place the first strong kinematic constraints on BCD evolutionary scenarios. The fact that the gaseous disks are supported by rotation, even for these most “dE-like” of the BCD class, implies that starbursting dwarf galaxies will not evolve passively into dwarf elliptical galaxies. However, since it is possible to transfer angular momentum via merging or interactions between galaxies, BCDs in high density regions could evolve into dwarf ellipticals via a more catastrophic evolutionary scenario. In fact, the formation of dwarf elliptical galaxies via ram pressure stripping of either gas-rich dwarf irregular galaxies or star-bursting dwarf galaxies is further substantiated by the strong morphology–density relationship

in low mass galaxies.

One potential concern is that the kinematic constraints presented here are for the gaseous disks of the starbursting dwarf galaxies, while the kinematic data for dwarf elliptical galaxies is almost entirely derived from observations of the stellar population. If the stars and gas are kinematically de-coupled in BCDs, the angular momentum arguments presented here are less compelling. In this regard, it is important to note that of the few dwarf ellipticals which have been mapped in HI, at least one, NGC 205, has a detectable velocity gradient in the gas disk (Young & Lo 1997) which is not detected in the stellar motions (Bender et al. 1991). Thus, further observations of the stellar kinematics of BCDs will be necessary to definitely exclude the possibility that BCDs evolve passively into dwarf elliptical galaxies when the starburst fades.

Nonetheless, the observed dynamics of BCDs appear to favor the hypothesis that post–burst BCDs should be found within the large, diverse, dwarf irregular classification. The definitive test of the BCD to dI evolutionary scenario will be to find examples of post–burst BCDs which have been classified as dwarf irregular galaxies. Studies of the structural parameters of dwarf irregular galaxies suggest that the majority of dIs are not related to the BCD class, but that a small percentage have similar morphology and color gradients (van Zee 2000, 2001). If these compact dIs are post–burst BCDs, they should also have similar gas distributions and gas dynamics as the BCDs. Thus, future HI synthesis observations of compact dIs should provide a direct test of the BCD to dI evolutionary scenario, and definitively determine if BCDs fade gracefully into more quiescent dIs, or if an altogether different, heretofore unknown, fate lies ahead.

We acknowledge the financial support by NSF grant AST95–53020 to JJS. Partial support from a NASA LTSARP grant No. NAGW–3189 (EDS) is gratefully acknowledged. This research has made use of the NASA/IPAC Extragalactic Database (NED) which is operated by the Jet Propulsion Laboratory, California Institute of Technology, under contract with the National Aeronautics and Space Administration.

REFERENCES

- Bender, R., & Nieto, J.–L. 1990, *A&A*, 239, 97
 Bender, R., Paquet, A., & Nieto, J.–L. 1991, *A&A*, 246, 349
 Briggs, D. 1995, PhD Thesis, New Mexico Tech
 Broeils, A. H., & Rhee, M.–H. 1997, *A&A*, 324, 877
 Broeils, A. H., & van Woerden, H. 1994, *A&AS*, 107, 129
 Carignan, C., & Beaulieu, S. 1989, *ApJ*, 347, 760
 Cole, S., Aragon–Salamanca, A., Frenk, C. S., Navarro, J. F., & Zepf, S. E. 1994, *MNRAS*, 271, 781
 Cole, S., Lacey, C. G., Baugh, C. M., & Frenk, C. S. 2000, *MNRAS*, 319, 168
 Cowie, L. L., Songalia, A., & Hu, E. M. 1991, *Nature*, 354, 460
 Davies, J. I., & Phillipps, S. 1988, *MNRAS*, 233, 553
 De Young, D. S., & Heckman, T. M. 1994, *ApJ*, 431, 598
 De Young, D. S., & Gallagher, J. S. 1990, *ApJ*, 356
 Dekel, A., & Silk, J. 1986, *ApJ*, 303, 39
 Doublier, V., Caulet, A., Comte, G. 1999, *A&AS*, 138, 213
 Doublier, V., Comte, G., Petrosian, A., Surace, C., & Turatto, M. 1997, *A&AS*, 124, 405
 Drinkwater, M., & Hardy, E. 1991, *AJ*, 101, 94
 Efstathiou, G. 2000, *MNRAS*, 317, 697
 Ferguson, H. C., & Babul, A. 1998, *MNRAS*, 296, 585
 Ferguson, H. C., & Binggeli, B. 1994, *A&A Rev.*, 6, 67
 Ferguson, H. C., & Sandage, A. 1989, *ApJ*, 346, 53
 Heckman, T. M., Dahlem, M., Lehnert, M. D., Fabbiano, G., Gilmore, D., & Waller, W. H. 1995, *ApJ*, 448, 98
 Heyl, J. S., Cole, S., Frenk, C. S., & Navarro, J. F. 1995, *MNRAS*, 274, 755
 Hoffman, G. L., Helou, G., Salpeter, E. E., & Lewis, B. M. 1989, *ApJ*, 339, 812
 Huchtmeier, W. K., & Richter, O. G. 1986, *A&AS*, 63, 323
 Iovino, A., Melnick, J., & Shaver, P. 1988, *ApJ*, 330, L17
 Izotov, Y. I., & Thuan, T. X. 1999, *ApJ*, 511, 639
 James, P. A. 1994, *MNRAS*, 269, 176
 Kauffmann, G., White, S. D. W., & Guiderdoni, B. 1993, *MNRAS*, 264, 201
 Kennicutt, R. C. 1989, *ApJ*, 344, 685
 Kennicutt, R. C. 1998, *ARA&A*, 36, 189
 Kormendy, J. 1985, *ApJ*, 295, 73
 Lee, J. C., Salzer, J. J., Law, D. A., & Rosenberg, J. L. 2000, *ApJ*, 536, 606
 Lin, D. N. C. & Faber, S. M. 1983, *ApJ*, 266, L21
 Loose, H.–H., & Thuan, T. X. 1985, in “Star-Forming Dwarf Galaxies and Related Objects” Kunth, D., Thuan, T. X., & Ván, T. T. eds. Paris: Editions Frontières, p. 73
 Loose, H.–H., & Thuan, T. X. 1986, *ApJ*, 309, 59
 Mac Low, M.–M., & Ferrara, A. 1999, *ApJ*, 513, 142

- Marlowe, A. T., Heckman, T. M., Wyse, R. F. G., & Schommer, R. 1995, *ApJ*, 438, 563
- Mateo, M. L. 1998, *ARA&A*, 36, 435
- Meurer, G. R., Carignan, C., Beaulieu, S. F., & Freeman, K. C. 1996, *AJ*, 111, 1551
- Meurer, G. R., Staveley-Smith, L., Killeen, N. E. B. 1998, *MNRAS*, 300, 705
- Moore, B. 1994, *Nature*, 370, 629
- Napier, P. J., Thompson, R. T., & Ekers, R. D. 1983, *Proc. IEEE*, 71, 1295
- Norton, S. A., & Salzer, J. J. 2001, in prep
- Papaderos, P., Loose, H.-H., Fricke, K. J., & Thuan, T. X. 1996a, *A&A*, 314, 59
- Papaderos, P., Loose, H.-H., Thuan, T. X., & Fricke, K. J. 1996b, *A&AS*, 120, 207
- Patterson, R. J., & Thuan, T. X. 1996, *ApJS*, 107, 103
- Pisano, D. J., & Wilcots, E. M. 1999, *AJ*, 117, 2168
- Pustil'nik, S. A., Ugryumov, A. V., Lipovetsky, V. A., Thuan, T. X., & Guseva, N. G. 1995, *ApJ*, 443, 499
- Putman, M. E., Bureau, M., Mould, J. R., Staveley-Smith, L. & Freeman, K. C. 1998, *AJ*, 115, 2345
- Rosenberg, J. L., Salzer, J. J., & Moody, J. W. 1994, *AJ*, 108, 1557
- Salzer, J. J., 2000, private communication
- Salzer, J. J., di Serego Alighieri, S., Matteucci, F., Giovanelli, R. & Haynes, M. P. 1991, *AJ*, 101, 1258
- Salzer, J. J., & Norton, S. A. 1999, in *IAU Colloquium 171: The Low Surface Brightness Universe*, ed. J. I. Davies, C. Impey, and S. Phillipps (ASP Conf. Series), 170, 253
- Salzer, J. J., Rosenberg, J. L., Weisstein, E., Mazzarella, J. M., & Bothun, G. D. 2001, submitted
- Sargent, W. L. W., & Searle, L. 1970, *ApJ*, 162, L155
- Schechter, P. 1980, *AJ*, 85, 801
- Silich, S. A., & Tenorio-Tagle, G. 1998, *MNRAS*, 299, 249
- Silk, J., Wyse, R. F. G., Shields, G. A. 1987, *ApJ*, 322, L59
- Simpson, C. E., & Gottesman, S. T. 2000, *AJ*, 120, 2975
- Skillman, E. D., & Bender, R. 1995, *Rev. Mex. AASC*, 3, 25
- Skillman, E. D., Bothun, G. D., Murray, M. A., & Warmels, R. H. 1987, *A&A*, 185, 61
- Somerville, R. S., & Primack, J. R. 1999, *MNRAS*, 310, 1087
- Sommer-Larsen, J., Gelato, S., & Vedel, H. 1999, *ApJ*, 519, 501
- Sung, E.-C., Han, C., Ryden, B. S., Chun, M.-S., & Kim, H.-I. 1998, *ApJ*, 499, 140
- Swaters, R. A., 1999, PhD Thesis, University of Groningen
- Taylor, C. L., Brinks, E., Grashius, R. M., & Skillman, E. D. 1995, *ApJS*, 99, 427
- Taylor, C. L., Brinks, E., Grashius, R. M., & Skillman, E. D. 1996, *ApJS*, 102, 189 (erratum)
- Taylor, C. L., Brinks, E., Pogge, R. W., & Skillman, E. D. 1994, *AJ*, 107, 971
- Terlevich, R., Melnick, J., Masegosa, J., Moles, M., & Copetti, M. V. F. 1991, *A&AS*, 91, 285
- Thuan, T. X., Izotov, Y. I., & Foltz, C. B. 1999, *ApJ*, 525, 105
- Toomre, A. 1964, *ApJ*, 139, 1217
- van der Hulst, J. M., Terlouw, J. P., Begemen, K., Zwitser, W., & Roelfsema, P. R. 1992, in *Astronomical Data Analysis Software and Systems*, ed. D. Worall, C. Biemesderfer, and J. Barnes (ASP Conference Series), 25, 131
- van Zee, L. 2000 *AJ*, 119, 2757
- van Zee, L. 2001 *AJ*, in press
- van Zee, L., Haynes, M. P., & Giovanelli, R. 1995, *AJ*, 109, 990
- van Zee, L., Haynes, M. P., Salzer, J. J., & Broeils, A. H. 1997b, *AJ*, 113, 1618
- van Zee, L., Skillman, E. D., & Salzer, J. J. 1998a, *AJ*, 116, 1186
- van Zee, L., Westpfahl, D., Haynes, M. P., & Salzer, J. J. 1998b, *AJ*, 115, 1000
- Walter, F., Brinks, E., Duric, N., & Klein, U. 1997, *AJ*, 113, 2031
- White, S. D. M., & Frenk, C. S. 1991, *ApJ*, 379, 52
- Wilcots, E. M., Lehman, C., & Miller, B. 1996, *AJ*, 111, 1575
- Young, L. M. 1999, *AJ*, 117, 1758
- Young, L. M. 2000, *AJ*, 119, 188
- Young, L. M., & Lo, K. Y. 1996, *ApJ*, 462, 203
- Young, L. M., & Lo, K. Y. 1997, *ApJ*, 476, 127

Table 1. Global Parameters

Galaxy	$\int Sdv$	V_0	W_{50}	Distance ^a	$\frac{D_{25} \times d_{25}^b}{[''] \quad [\text{kpc}]}$			M_{HI}	$\frac{D_{\text{HI}}}{D_{25}}$	$M_{\text{HI}}/L_{\text{B}}$	SFR^b	Log	12 +	L-band
	[Jy km s ⁻¹]	[km s ⁻¹]	[km s ⁻¹]		[Mpc]	['']	[kpc]	M_{B}^b	[10 ⁸ M _⊙]	[M _⊙ /L _⊙]	[M _⊙ yr ⁻¹]	(M _{HI} /SFR)	log(O/H) ^c	cont. emission
UM 38	2.99	1378	121	20.3	32×24	3.1×2.4	-16.04	2.90	2.2	0.72	0.038	9.88	8.15±0.20	1.0 ± 0.1
UM 323	2.52	1915	59	26.7	24×16	3.1×2.1	-16.05	4.23	2.4	1.03	0.111	9.58	7.70±0.20	0.3 ± 0.1
MK 1418	8.38	759	105	10.8	48×33	2.5×1.7	-15.80	2.30	2.3	0.71	3.9 ± 0.3
MK 750	1.91	756	51	8.8	27×19	1.2×0.8	-14.23	0.35	2.0	0.46	0.052	8.83	8.11±0.02	1.7 ± 0.1
MK 900	2.03	1155	140	18.0	44×36	3.8×3.1	-17.14	1.55	1.2	0.21	0.088	9.24	8.74±0.20	1.3 ± 0.1
MK 324	2.34	1600	121	24.4	29×23	3.4×2.7	-16.73	3.28	1.9	0.50	0.065	9.70	8.50±0.20	1.4 ± 0.1

^aDistances computed using a Virgocentric infall model assuming $H_0=75 \text{ km s}^{-1} \text{ Mpc}^{-1}$, a Virgo infall velocity of 300 km s^{-1} , and an overdensity of 2.

^bDoublier et al. (1997); van Zee (2000); Salzer et al. (2001).

^cTerlevich et al. (1991); Izotov & Thuan (1999); Salzer, private communication.

Table 2. HI Synthesis Imaging Observing Log

Galaxy	Date	Configuration	T_{int} [min]
UM 38	1998 Aug 5	B	167.0
	1998 Aug 16	B	367.5
	1998 Dec 21	CS	274.5
UM 323	1998 Aug 19	B	175.0
	1998 Oct 9	B	356.5
	1999 Jan 22	CS	269.0
MK 1418	1999 Dec 10	B	112.5
	1999 Dec 11	B	107.5
	2000 May 25	CS	99.5
MK 750	1999 Dec 10	B	466.0
	2000 May 25	CS	183.5
MK 900	1998 Aug 5	B	360.5
	1998 Aug 16	B	169.0
	1998 Dec 7	CS	271.5
MK 324	1998 Aug 19	B	356.5
	1998 Oct 9	B	162.0
	1998 Dec 11	CS	272.0

Table 3. Parameters of the HI Data Cubes

Galaxy	Robustness	uv taper		uv range		Beam	rms	N_{H} sensitivity ^a	linear
	Parameter	[k λ k λ]		[k λ k λ]		[arcsec \times arcsec]	[mJy beam ⁻¹]		resolution
UM 38	5	15	15	0	20	18.5×15.8	0.54	3×10^{19}	1.82×1.55
	5		10.4×8.4	0.50	1×10^{20}	1.02×0.83
	0.5		7.0×5.4	0.58	3×10^{20}	0.69×0.53
UM 323	5	15	15	0	20	17.4×15.6	0.54	3×10^{19}	2.25×2.02
	5		9.6×8.8	0.50	1×10^{20}	1.24×1.14
	0.5		6.5×6.0	0.58	3×10^{20}	0.84×0.78
MK 1418	5	15	15	0	20	15.7×15.2	0.70	5×10^{19}	0.82×0.80
	5		7.9×7.6	0.51	1×10^{20}	0.41×0.40
	0.5		5.6×5.5	0.55	3×10^{20}	0.29×0.29
MK 750	5	15	15	0	20	16.1×15.5	0.62	4×10^{19}	0.69×0.66
	5		8.7×7.7	0.50	1×10^{20}	0.37×0.33
	0.5		6.0×5.4	0.58	3×10^{20}	0.26×0.23
MK 900	5	15	15	0	20	17.0×15.9	0.61	4×10^{19}	1.48×1.39
	5		8.6×7.8	0.49	1×10^{20}	0.75×0.68
	0.5		5.9×5.4	0.54	3×10^{20}	0.51×0.47
MK 324	5	15	15	0	20	16.7×15.7	0.40	3×10^{19}	1.98×1.86
	5		9.4×7.7	0.36	9×10^{19}	1.11×0.91
	0.5		6.1×5.2	0.42	2×10^{20}	0.72×0.62

^aColumn density sensitivity has been calculated assuming a 3 sigma detection in 2 consecutive channels.

Table 4. Parameters of Other Galaxies in the Fields

Galaxy	RA (1950)	Dec (1950)	D _{center} ^a [arcmin]	$\int S dv$ [Jy km s ⁻¹]	V ₀ [km s ⁻¹]	W ₅₀ [km s ⁻¹]	Distance [Mpc]	M _{HI} [10 ⁸ M _⊙]
EXG0123–0040	01 23 42.7	–00 40 04	16.0	0.68	1941.6	38	27.1	1.18
EXG2323+1816	23 23 23.8	18 16 15	18.1	1.81	1506.6	50	23.1	2.27

^aDistance from pointing center to the galaxy.

Table 5. Peak Gas Densities

Galaxy	N_{HI} [10^{21} cm^{-2}]	Σ_g^a		$< \Sigma_c >$		resolution [kpc beam $^{-1}$]
		[10^{21} cm^{-2}]	[$M_{\odot} \text{ pc}^{-2}$]	[10^{21} cm^{-2}]	[$M_{\odot} \text{ pc}^{-2}$]	
UM 38	3.13	3.20	25.6	3.3	27	0.69×0.53
	2.72	2.78	22.2			1.02×0.83
	1.90	1.94	15.5			1.82×1.55
UM 323	3.48	3.39	27.1	0.84×0.78
	2.79	2.72	21.8			1.24×1.14
	1.98	1.93	15.4			2.25×2.02
MK 1418	3.06	2.28	18.2	4.3	34	0.41×0.40
	4.14	3.08	24.6			0.41×0.40
	3.07	2.28	18.3			0.29×0.29
MK 750	1.33	1.45	11.6	6.5	52	0.69×0.66
	2.12	2.31	18.5			0.37×0.33
	2.81	3.06	24.5			0.26×0.23
MK 900	2.58	2.52	20.1	3.4	27	0.51×0.47
	2.17	2.12	16.9			0.75×0.68
	1.64	1.60	12.8			1.48×1.39
MK 324	2.95	3.10	24.8	0.72×0.62
	2.48	2.60	20.8			1.11×0.91
	1.56	1.64	13.1			1.98×1.86
B0123-0040	1.12	1.26×1.16
	0.52			2.29×2.05
B2323+1816	2.73	1.05×0.86
	1.31			1.87×1.76

^a Σ_g has been corrected for inclination and neutral helium content.

Table 6. Kinematic Parameters

Galaxy	Kinematic Center		Systemic Velocity [km s ⁻¹]	<PA> [deg]	<i> [deg]	R _{max} [kpc]	V(R _{max}) [km s ⁻¹]	M _{dyn} [10 ⁸ M _⊙]	$\frac{M_{\text{HI}}}{M_{\text{dyn}}}$	< σ > [km s ⁻¹]
	RA (1950)	Dec (1950)								
UM 38	00 25 17.3	03 12 47	1381	268 ± 3	40 ± 5	2.95	76.7	40.4	0.07	9 ± 4
UM 323	01 24 13.1	-00 54 18	1921	264 ± 10	43 ± 10	1.75:	42.8:	7.5:	0.57:	8 ± 3
MK 1418	09 37 09.4	48 33 49	773	228 ± 10	56 ± 10	2.09:	37.7:	6.91:	0.33:	9 ± 3
MK 750	11 47 28.2	15 18 08	757	175 ± 10	35 ± 10	0.47:	71.0:	5.51:	0.06	7 ± 3
MK 900	21 27 27.5	02 11 40	1145	59 ± 3	43 ± 5	1.05	82.0	16.4	0.09	7 ± 2
MK 324	23 24 02.4	17 59 29	1601	167 ± 10	38 ± 10	2.36:	92.8:	47.3:	0.07:	7 ± 2